

High-resolution enviromagnetic records of the last deglaciation from Dali Lake, Inner Mongolia



Suzhen Liu^{a,b}, Chenglong Deng^{a,b,*}, Jule Xiao^c, Jinhua Li^d, Greig A. Paterson^d, Liao Chang^e, Liang Yi^a, Huafeng Qin^a, Rixiang Zhu^a

^a State Key Laboratory of Lithospheric Evolution, Institute of Geology and Geophysics, Chinese Academy of Sciences, Beijing 100029, China

^b University of Chinese Academy of Sciences, Beijing 100049, China

^c Key Laboratory of Cenozoic Geology and Environment, Institute of Geology and Geophysics, Chinese Academy of Sciences, Beijing 100029, China

^d Key Laboratory of Earth and Planetary Physics, Institute of Geology and Geophysics, Chinese Academy of Sciences, Beijing 100029, China

^e Research School of Earth Sciences, The Australian National University, Canberra, ACT 0200, Australia

ARTICLE INFO

Article history:

Received 31 October 2015

Received in revised form 25 March 2016

Accepted 11 April 2016

Available online 16 April 2016

Keywords:

Semi-arid East Asia

Dali Lake

Last deglaciation

Paleoclimate

Environmental magnetism

ABSTRACT

Detailed paleoclimate records during the last deglaciation are highly valuable for understanding rapid climatic changes and mechanisms during extremely variable conditions. High-resolution paleoclimate research in the semi-arid East Asian interior is essential due to its sensitivity to climate variability and importance for human inhabitation. A high-resolution environmental magnetic investigation has been performed on a sedimentary sequence from Dali Lake in central Inner Mongolia, which covers the period of 15.90–11.46 ka. Variable magnetic mineral sources are identified based on integrated rock magnetic analysis of both core sediments and catchment samples, complemented by scanning electron telescope and transmission electron telescope observation and X-ray diffraction analysis. The studied core is magnetically divided into four units: Magnetic minerals in Unit 1 (11.83–11.5 m, 15.90–15.32 ka) are mainly sourced from bedrock erosion of basalts in the catchment. This period corresponds to rapid climate fluctuations after the Last Glacial Maximum. In Unit 2 (11.50–9.50 m, 15.32–12.67 ka) and Unit 3 (9.50–8.59 m, 12.67–11.56 ka), pseudo-single domain magnetites from erosion of surface soils are the main magnetic carriers. These two units coincide within time error with the Bølling–Allerød warm period and the Younger Dryas cold period, respectively, and can be correlated with stalagmite and ice core records. Our findings reflect contrasting erosion processes during cold and warm periods in the lake catchment, which were ultimately controlled by climate changes during the last deglaciation.

© 2016 Elsevier B.V. All rights reserved.

1. Introduction

The last deglaciation represents the youngest transition from glacial to interglacial climate stages. Study of the last deglaciation is important for understanding the natural background during extreme climate changes (Ruddiman, 2014). Attention has been paid to rapid climate oscillations during the last deglaciation since the discovery of Heinrich events and Dansgaard–Oeschger cycles (Dansgaard et al., 1993; Heinrich, 1988). Although significant advance has been made based on archives in Greenland ice cores (Stuiver et al., 1995) and North Atlantic marine sediments (Bond et al., 1993), reports of these climatic oscillations in continental Europe (Thouveny et al., 1994) and East Asia (Yuan et al., 2004) suggest their global occurrence.

Semi-arid East Asia is of great interest for paleoenvironment and paleoclimate studies (An et al., 2015). Research in this region on

tectonic (Guo et al., 2002), orbital (Deng et al., 2006; Ding et al., 2002; Hao et al., 2015; Heller and Liu, 1984) and millennial scales (Ding et al., 1998; Guo et al., 1996; Porter and An, 1995) has provided a wealth of information on global and regional climate changes. The climate instability during the last deglaciation in semi-arid East Asia was mostly reported in the Loess Plateau (Ding et al., 1998; Guo et al., 1996; Zhou et al., 1999). By comparing the Chinese loess grain size with Greenland Ice-core Project (GRIP) ice core $\delta^{18}\text{O}$ and *Neogloboquadrina pachyderma* (s.) abundance in North Atlantic sediments, Porter and An (1995) proposed teleconnection between East Asia winter monsoon and North Atlantic oceanic conditions during the last glaciation. Subsequently, Guo et al. (1996) further documented this climate teleconnection through analyzing chemical weathering indices of Chinese loess and extended this behavior into the penultimate glaciation. Recently, several high-resolution enviromagnetic records on lake sediments in the semi-arid East Asia depicted climate fluctuations during the last deglaciation and Holocene (Chen et al., 2013; Liu et al., 2011, 2015; Tang et al., 2015). Given their locations at the East Asian summer monsoon limit, these lakes are highly sensitive to climate changes. Therefore, detailed

* Corresponding author at: State Key Laboratory of Lithospheric Evolution, Institute of Geology and Geophysics, Chinese Academy of Sciences, Beijing 100029, China.

E-mail address: cldeng@mail.iggcas.ac.cn (C. Deng).

variations between climatic extremes documented in these records are essential to explore future global changes of both natural and anthropogenic origin.

In this study, we present a high-resolution Dali Lake sediment record of the last deglaciation in Inner Mongolia, northern China. The 11.83-m core DL04 was drilled in 2004. Results of the upper 8.5 m (0–11.5 ka) have been described in Liu et al. (2015), which documented a biomagnetic response recorded as magnetofossils to the Holocene Warm Period. Here, the lower part of the core was systematically studied using multi-parameter rock magnetic methods. Based on changes in magnetic mineralogy, concentration and grain size, we have investigated the magnetic mineral sources and depositional processes. We

interpret these magnetic changes as representing rapid climate fluctuations during the last deglaciation.

2. Geological setting, sampling and chronology

Dali Lake ($43^{\circ}13'–23' \text{ N}$, $116^{\circ}29'–45' \text{ E}$, $\sim 1230 \text{ m a.s.l.}$) is an inland closed-basin lake in central Inner Mongolia (Fig. 1). It currently has an area of 238 km^2 and a maximum water depth of 11 m. The lake floor has a steep slope near the shore and an almost flat bottom toward the center. Given its location just at the modern limit of the East Asian summer monsoon (Fig. 1a), the lake sedimentation process should be highly sensitive to monsoon variability. Therefore, the lake sediments provide

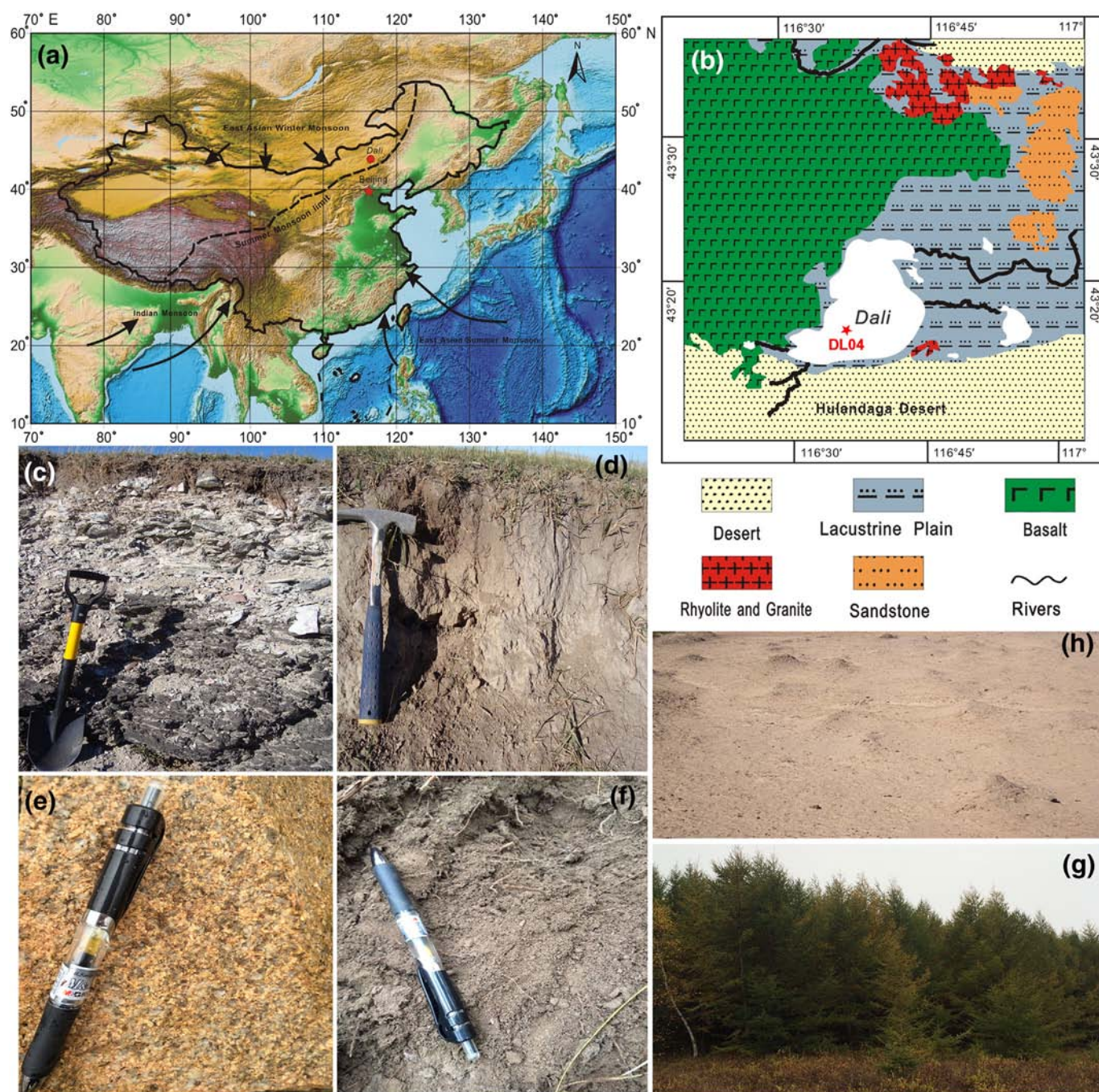


Fig. 1. Geological setting of Dali Lake, core position and catchment samples. a, Regional atmospheric circulations (arrows, the East Asian summer monsoon, East Asian winter monsoon and Indian Monsoon) and modern summer monsoon limit (dashed line); b, geological setting of Dali Lake; c–h, photographs of catchment samples. c, Basalt; d, grassland soils around the lake; e–g, granite, forests and forest soils at the Huanggangliang highland at the headwater areas. The Huanggangliang highland is about 80 km northeast of Dali Lake, with its peak at $43^{\circ}34' \text{ N}$, $117^{\circ}37' \text{ E}$, $\sim 1770 \text{ m a.s.l.}$; h, sand dunes in Hulandaga Desert.

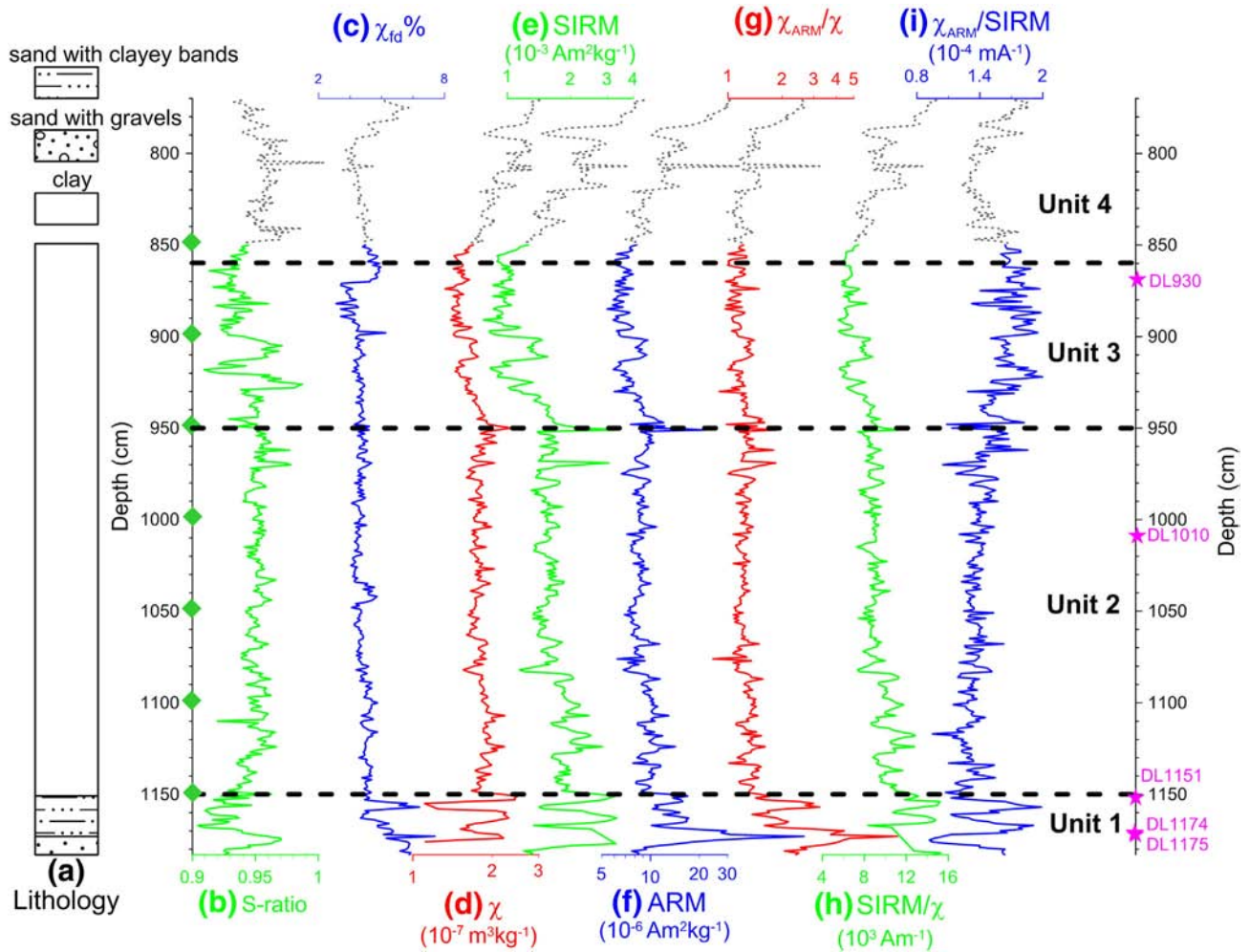


Fig. 2. Lithology and magnetic parameter changes vs depth for Dali Lake. a, Lithology of the studied core sediments; b, S-ratio, which indicates homogeneity in magnetic mineralogy; c, the relative frequency-dependent magnetic susceptibility ($\chi_{fd}\%$); d–f, magnetic concentration parameters; g–i, ratios used as magnetic grain size proxies. Differences between the three ratios stem from distinctive sensitivity to different grain size ranges. Note that d–g are plotted on a logarithmic scale. The sequence is divided into four units based on changes in lithology and magnetic parameters. Positions of representative samples are shown on the right by stars. Depths of samples used for accelerator mass spectrometer radiocarbon dating results are shown on the left by diamonds. Data over the depth interval of 8.50–7.70 m (dotted lines) are after Liu et al. (2015).

valuable paleoclimate archives due to monsoonal changes (Fan et al., 2015; Xiao et al., 2008, 2009). Pleistocene basaltic rocks surround the lake to the north and west. The E–W trending Hulandaga Desert lies to the south. Along the eastern shore are lacustrine plains (Fig. 1b).

The studied DL04 sediment core ($43^{\circ}15.68' \text{ N}$, $116^{\circ}36.26' \text{ E}$, Fig. 1b) was drilled at the depocenter in 2004 as described in Xiao et al. (2008). The core was split and cut on site at 1-cm intervals. Core sediments between 8.5 m and 11.83 m were used for this study and a total of 333 powdered samples were obtained. The cored sediments from 8.5 m to 11.5 m are composed of blackish-gray homogeneous clays and silty clays. Sediments in the lower part from 11.5 m to 11.83 m contain black and gray sands. Clayey bands are found from 11.5 m to 11.73 m, and small gravels can be seen in sediments between 11.73 m and 11.83 m (Fig. 2a).

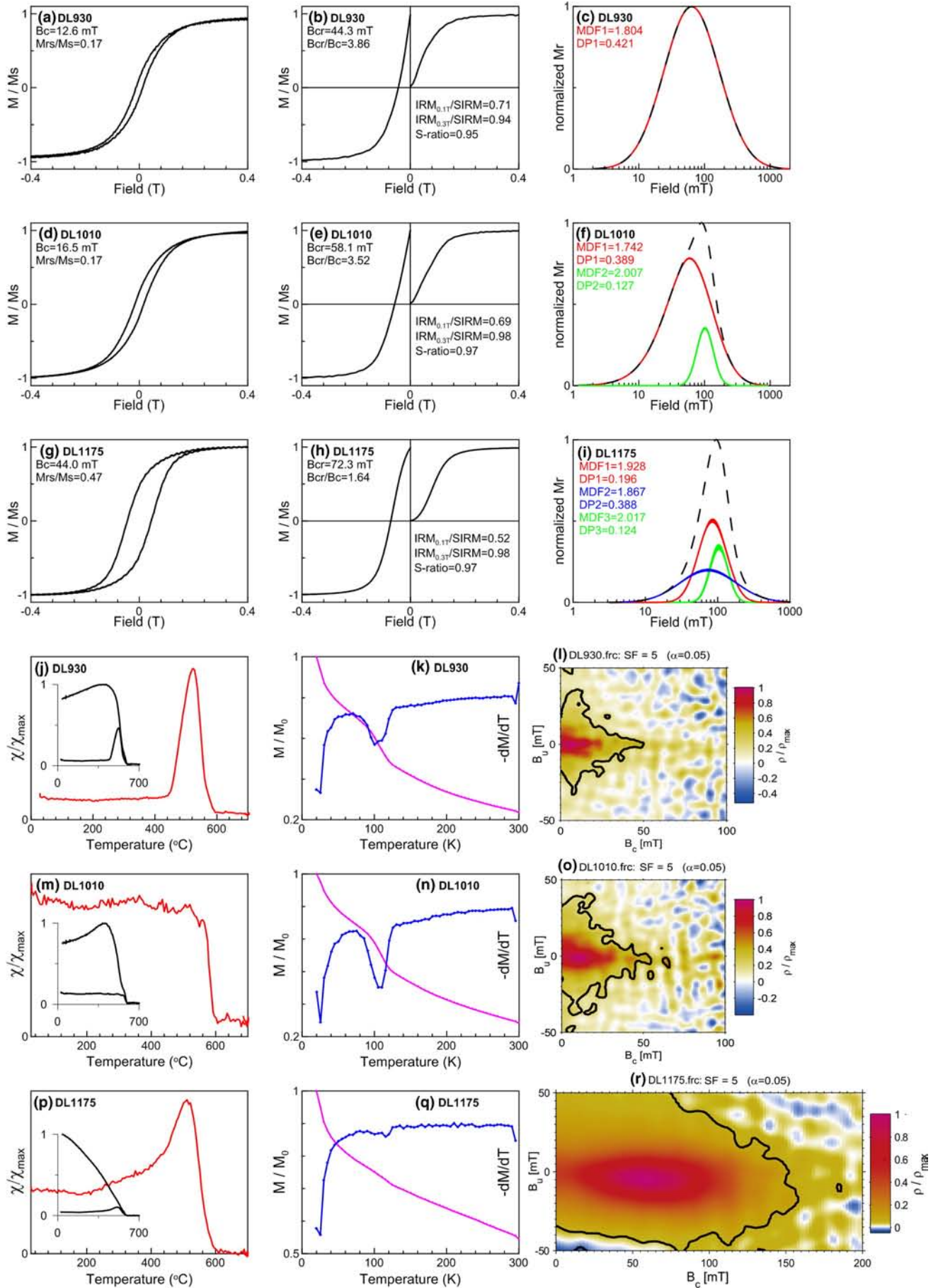
The core sediments in this study are divided into four units according to changes in lithology and magnetic features (Fig. 2): Unit 1 (11.83–11.50 m, 15.90–15.32 ka), Unit 2 (11.50–9.50 m, 15.32–12.67 ka), Unit 3 (9.50–8.59 m, 12.67–11.56 ka) and Unit 4 (8.59–7.70 m, 11.56–10.00 ka). Three representative core sediment samples are analyzed in detail, which include DL1175 (11.75 m, 15.76 ka) from Unit 1, DL1010 (10.10 m, 13.16 ka) from Unit 2 and DL930 (9.30 m, 12.40 ka) from Unit 3. Moreover, catchment samples were collected during field investigation and drilling process, including bedrocks, surface soils and eolian dust which are potential detrital

sources for the Dali Lake sediments and associated magnetic minerals. The catchment samples analyzed in this study include granite and forest soils at the Huanggangliang highland in the headwater areas, Pleistocene vesicular basalt from western and northern parts of the lake, grassland soils around the lake, sand dunes at the southern shore of the lake, and eolian dust collected on ice when the lake is frozen in winter. We have collected and analyzed about 130 samples at 41 sites, and results of one representative catchment sample of each category are shown in Section 4.3.

Chronology is based on linear interpolation between seven accelerator mass spectrometer radiocarbon dates on bulk samples (Table 1). The 3.33-m studied core covers a 4.43-kyr-period from 15.90 ka to 11.46 ka.

Table 1
Radiocarbon dating results. AMS is for accelerator mass spectrometer.

Lab number	Depth (cm)	$\delta^{13}\text{C}$ (‰)	AMS ^{14}C age (^{14}C yr BP)	Calibrated ^{14}C age (2 σ) (cal yr BP)
PLD-12472	848.5	-30.84 ± 0.19	$10,464 \pm 37$	11,640–11,268
PLD-12474	898.5	-27.92 ± 0.19	$10,715 \pm 34$	12,142–11,815
PLD-12477	949.5	-31.40 ± 0.13	$11,050 \pm 35$	12,785–12,560
PLD-12478	998.5	-31.97 ± 0.22	$11,630 \pm 38$	13,166–12,946
PLD-12480	1049	-30.63 ± 0.14	$12,158 \pm 37$	13,676–13,411
PLD-12483	1100	-27.39 ± 0.22	$12,876 \pm 42$	14,797–14,141
PLD-13857	1150	-27.78 ± 0.20	$13,436 \pm 39$	15,609–15,049



3. Methods

Magnetic measurements were carried out on the 333 bulk sediment samples. The samples were first dried in vacuum and embedded into standard 8-cm³ cubic boxes. Magnetic susceptibility (χ) was measured using an AGICO MFK1-FA Multi-Frequency Kappabridge magnetic susceptibility meter at frequencies of 976 Hz and 15,616 Hz. The relative frequency-dependent magnetic susceptibility ($\chi_{fd}\%$) was calculated as $(\chi_{976 \text{ Hz}} - \chi_{15616 \text{ Hz}}) / \chi_{976 \text{ Hz}} \times 100\%$. Anhysteretic remanent magnetization (ARM) was imparted using a peak alternating field (AF) of 100 mT and a direct bias field of 0.05 mT using a 2-G Enterprises SQUID magnetometer with inline AF coils. Isothermal remanent magnetization (IRM) was induced with a 2-G Enterprises model 660 pulse magnetizer successively in pulsed fields of 1 T (IRM_{1 T}, hereafter termed SIRM, the saturation IRM) and -0.3 T (IRM_{-0.3 T}). S-ratio, which is defined as the ratio of IRM_{-0.3 T} to SIRM (King and Channell, 1991), was determined to estimate the relative contributions of low-coercivity magnetic minerals (e.g., magnetite and/or maghemite) over high-coercivity magnetic minerals (e.g., hematite and/or goethite). All remanence measurements were measured using the 2-G magnetometer.

For representative samples from core sediments and catchment samples, detailed rock magnetic properties were measured as follows: 1) Hysteresis loops, IRM acquisition, back-field demagnetization of SIRM, and first-order reversal curves (FORCs) were measured with a Princeton Measurements Corporation MicroMag 3900 vibrating sample magnetometer (VSM, sensitivity = $0.5 \times 10^{-9} \text{ Am}^2$) up to a maximum field of 1 T. FORC diagrams were calculated using the FORCme software package (Heslop and Roberts, 2012). Magnetic components were analyzed using the unmixing programs written by Egli (2003). 2) High-temperature magnetic susceptibility measurements (χ - T curves) were performed in an argon atmosphere using an AGICO MFK1-FA equipped with CS-3 temperature control system. The temperature ranges from 25 °C to 700 °C with a ramping rate of 2 °C/min. 3) Low-temperature magnetic measurements were performed on a Quantum Design Magnetic Property Measurement System (MPMS-XL, sensitivity = $5.0 \times 10^{-10} \text{ Am}^2$). Samples were first cooled from 300 K to 20 K in zero fields (ZFC). At 20 K an SIRM was imparted with a 2.5 T field (hereafter termed SIRM_{20K,2.5 T}) and then the remanence was measured during zero field warming to 300 K.

To better identify the mineralogy and grain size of the magnetic minerals from Unit 1, two representative samples (DL1150 at 11.51 m, 15.35 ka; DL1174 at 11.74 m, 15.74 ka) were magnetically extracted and analyzed by scanning electron telescope (SEM), transmission electron telescope (TEM) and energy dispersive spectra (EDS). Extraction was performed in the same way as described in Liu et al. (2015). SEM experiments were carried out on a LEO1450VP SEM equipped with an INCA ENERGY 300 X-ray EDS. TEM was performed on a JEOL-2100F microscope. All the magnetic and SEM experiments were made at the Institute of Geology and Geophysics, Chinese Academy of Sciences.

In addition, representative bulk samples from the DL04 core and the lake catchment were analyzed by X-ray diffraction (XRD). All samples were ground to <45 μm with an agate mortar before separated on glass slides to obtain oriented mounts. XRD was performed on a PANalytical X'Pert PRO diffractometer at 40 kV and 40 mA. The scanning angle ranged from 0 to 90°. The XRD results were analyzed using the X'Pert Highscore software.

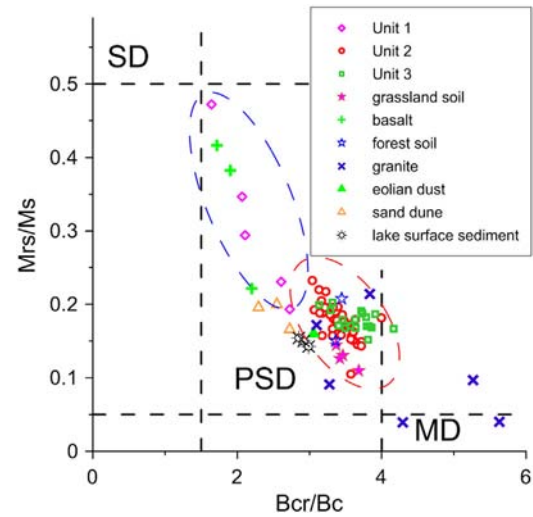


Fig. 4. Day plot of representative core sediments and catchment materials. Every fifth sample for the core sediments and one representative for the catchment samples are shown. Samples from Unit 1 and catchment basalt cluster in the upper left-hand corner, which indicates SD-like behavior. Samples from Unit 2, Unit 3 and surface soils cluster in the lower right-hand corner, implying PSD- or MD-like behavior. SD stands for single domain, PSD for pseudo-single domain, and MD for multidomain.

4. Results

4.1. Time series of rock magnetic parameters

High S-ratio values (above 0.90) indicate the dominance of low-coercivity magnetic minerals throughout the whole sequence (Fig. 2b). The concentration-dependent magnetic parameters (χ , ARM and SIRM) have similar variations throughout the core, which suggests that these proxies are not greatly influenced by mineralogical variations (Fig. 2d–f). Based on the general variations of the concentration-dependent magnetic parameters (χ , ARM and SIRM) and the grain-size-dependent rock magnetic parameters (χ_{ARM}/χ , $\chi_{\text{ARM}}/\text{SIRM}$ and SIRM/χ), the magnetic series was divided into four units, Units 1 to 4, from bottom to top.

4.1.1. Unit 1 (11.83–11.50 m, 15.90–15.32 ka)

In Unit 1, all three concentration-dependent parameters show high-amplitude fluctuations, with three peaks at 11.51 m (15.35 ka), 11.60 m (15.50 ka) and 11.73 m (15.72 ka) (Fig. 2d–f). Values of χ_{ARM}/χ , $\chi_{\text{ARM}}/\text{SIRM}$ and SIRM/χ also have large fluctuations and peak at the depths where magnetic concentrations are high (Fig. 2g–i), which implies relatively fine magnetic grains in these highly-magnetic layers. Changing $\chi_{fd}\%$ values (~4% to 8%) suggest variable contributions of superparamagnetic (SP) particles in Unit 1 (Fig. 2c).

4.1.2. Unit 2 (11.50–9.50 m, 15.32–12.67 ka)

All three magnetic concentration parameters for Unit 2 have low values compared with Unit 1, reflecting a lower magnetic concentration in this unit (Fig. 2d–f). Values of $\chi_{\text{ARM}}/\text{SIRM}$, which excludes the contribution from SP particles, have an up-section increasing trend (Fig. 2i). This may indicate decreasing coarse-grained pseudo-single domain (PSD) or multi-domain (MD) particles in Unit 2. On the contrary, values of χ_{ARM}/χ and SIRM/χ , which are influenced by SP particles, decrease

Fig. 3. Rock magnetic results for representative core sediments, including hysteresis loops (a, d, g), IRM acquisition and DC demagnetization curves (b, e, h), unmixing of the IRM acquisition curves (c, f, i), magnetic susceptibility vs temperature curves during heating (χ - T , j, m, p), SIRM_{20K,2.5 T} vs temperature curves (k, n, q) and first-order reversal diagrams (FORCs) which are calculated with a smoothing factor (SF) of 5 (l, o, r). The hysteresis loops and IRM curves, which are obtained in the applied field up to 1 T, are cut off at 0.4 T for clarity. For χ - T , the heating and cooling curves together are shown as insets; only the heating curves are shown in red; magnetic susceptibilities during heating and cooling are normalized with the maximum values. For the SIRM_{20K,2.5 T} vs temperature curves, triangles represent the magnetizations (normalized by the remanent magnetization at 20 K), and diamonds represent first derivative of magnetizations with respect to temperature. (For interpretation of the references to color in this figure legend, the reader is referred to the web version of this article.)

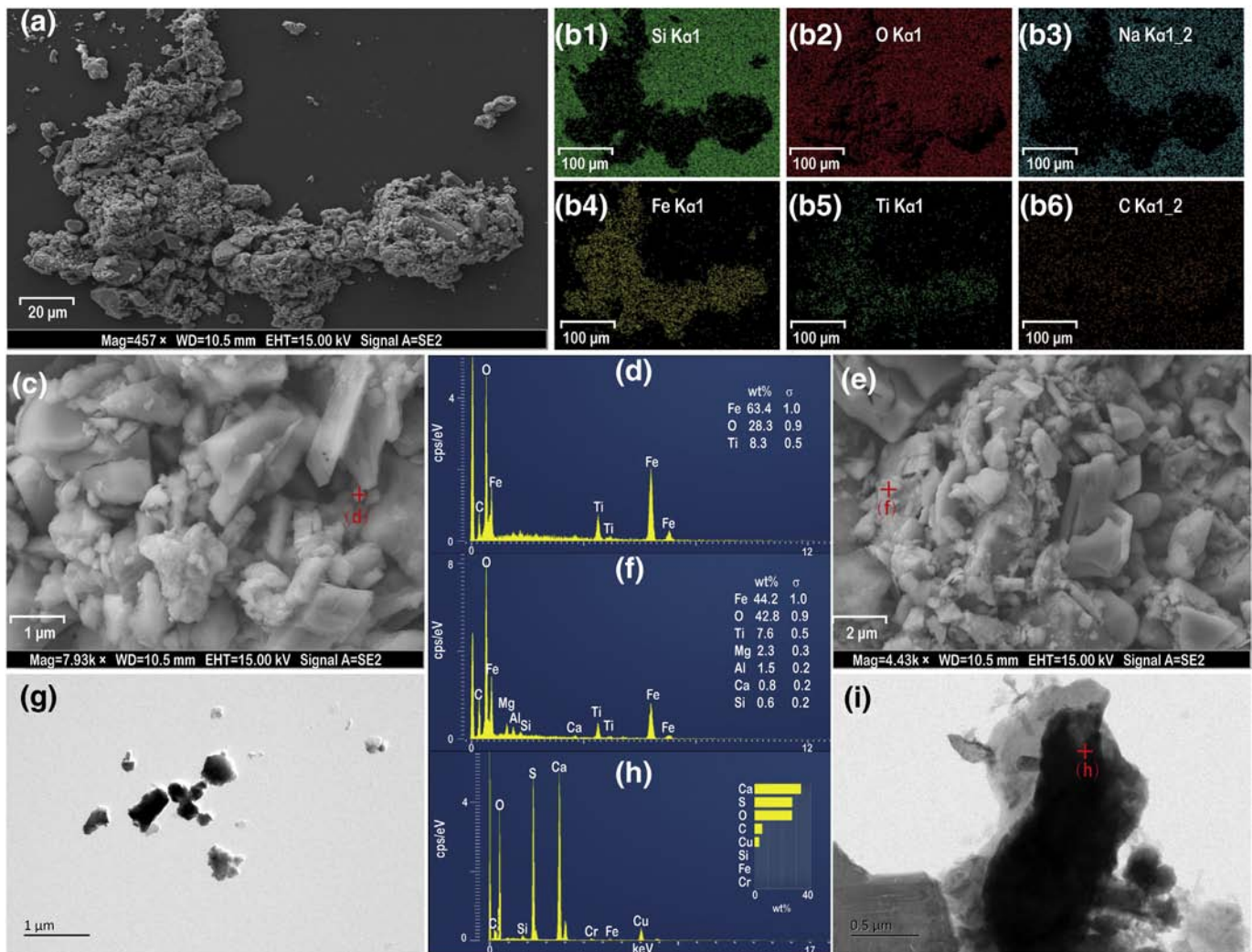


Fig. 5. SEM, TEM and EDS results for the representative samples in Unit 1 (a–f, DL1151 at 11.51 m, 15.35 ka; g–i, DL1174 at 11.74 m, 15.74 ka). a, c, e, Backscattered electron images under SEM; g, i, backscattered electron images under TEM; b1–b6 are scanning maps for a; d, f, h are EDS results, positions of which are shown by crosses.

up-section (Fig. 2g, h). The different variations between these three parameters may be due to increasing contribution of SP particles in the upper part of the section, which contribute to χ but not to ARM and SIRM. The $\chi_{rd}\%$ values show an insignificant upward increase (Fig. 2c), which is, however, not contradictory with our explanation since $\chi_{rd}\%$ value is only sensitive to a certain grain size range of SP particles. Overall, the grain-size indicators suggest an up-section fining trend in magnetic grain size in Unit 2 with less coarse PSD or MD but more SP particles in the upper part.

4.1.3. Unit 3 (9.50–8.59 m, 12.67–11.56 ka)

Unit 3 has the lowest values of χ , ARM and SIRM, indicative of the lowest magnetic concentration (Fig. 2d–f). Similar to Unit 2, the three magnetic grain size parameters have different trends. Compared with Unit 2, χ_{ARM}/χ values are higher in Unit 3, but χ_{ARM}/χ and SIRM/ χ values are lower (Fig. 2g–i). One explanation for this difference is an increase of fine SP particles but decrease of coarse PSD or MD magnetic grains in Unit 3. This inferred change is consistent with an obviously clear decrease in SIRM (Fig. 2e) and slightly decrease in χ and ARM values (Fig. 2d, f).

4.1.4. Unit 4 (8.59–7.70 m, 11.56–10.00 ka)

Samples in Unit 4 have nearly the same magnetic properties with their counterparts in Unit 2. Magnetic concentration is higher in Unit 4 than in Unit 3, but obviously lower than in Unit 1 (Fig. 2d–f). Magnetic

grain size in Unit 4 is coarser than in Unit 3 (Fig. 2g–i). The upper part of Unit 4 from the early Holocene (Liu et al., 2015) is included here to better illustrate the trend of the magnetic parameters, but Unit 4 is not discussed in detail in this paper.

4.2. Magnetic and non-magnetic properties of representative core sediments

4.2.1. Hysteresis properties and FORC diagrams

Hysteresis loops after paramagnetic correction are closed above 0.3 T (Fig. 3a, d, g), and both IRM acquisition curves reach saturation after 0.3 T (Fig. 3b, e, h), which implies the dominance of low-coercivity ferrimagnetic minerals. Hysteresis parameters indicate that DL1175 from Unit 1 has $B_c > 30$ mT and $B_{cr} > 60$ mT (Fig. 3g, h), and projection on the Day plot (Day et al., 1977) near the single domain (SD) area (Fig. 4). Remanence unmixing (Egli, 2003) reveals three components, the main of which is narrow ($DP = 0.196$) at ~ 85 mT (Fig. 3i). For DL1010 from Unit 2 and DL930 from Unit 3, B_c and B_{cr} have lower values of 10–20 mT and 40–60 mT, respectively (Fig. 3a, b, d, e). Samples in Units 2 and 3 both cluster in the lower right-hand corner of the PSD region of the Day plot (Fig. 4). The main magnetic component after unmixing is widely distributed ($DP > 0.3$) and is centered at ~ 60 mT (Fig. 3c, f).

FORC diagrams display a range of coercivity spectra and magnetic interaction fields among the magnetic particles (Roberts et al., 2000,

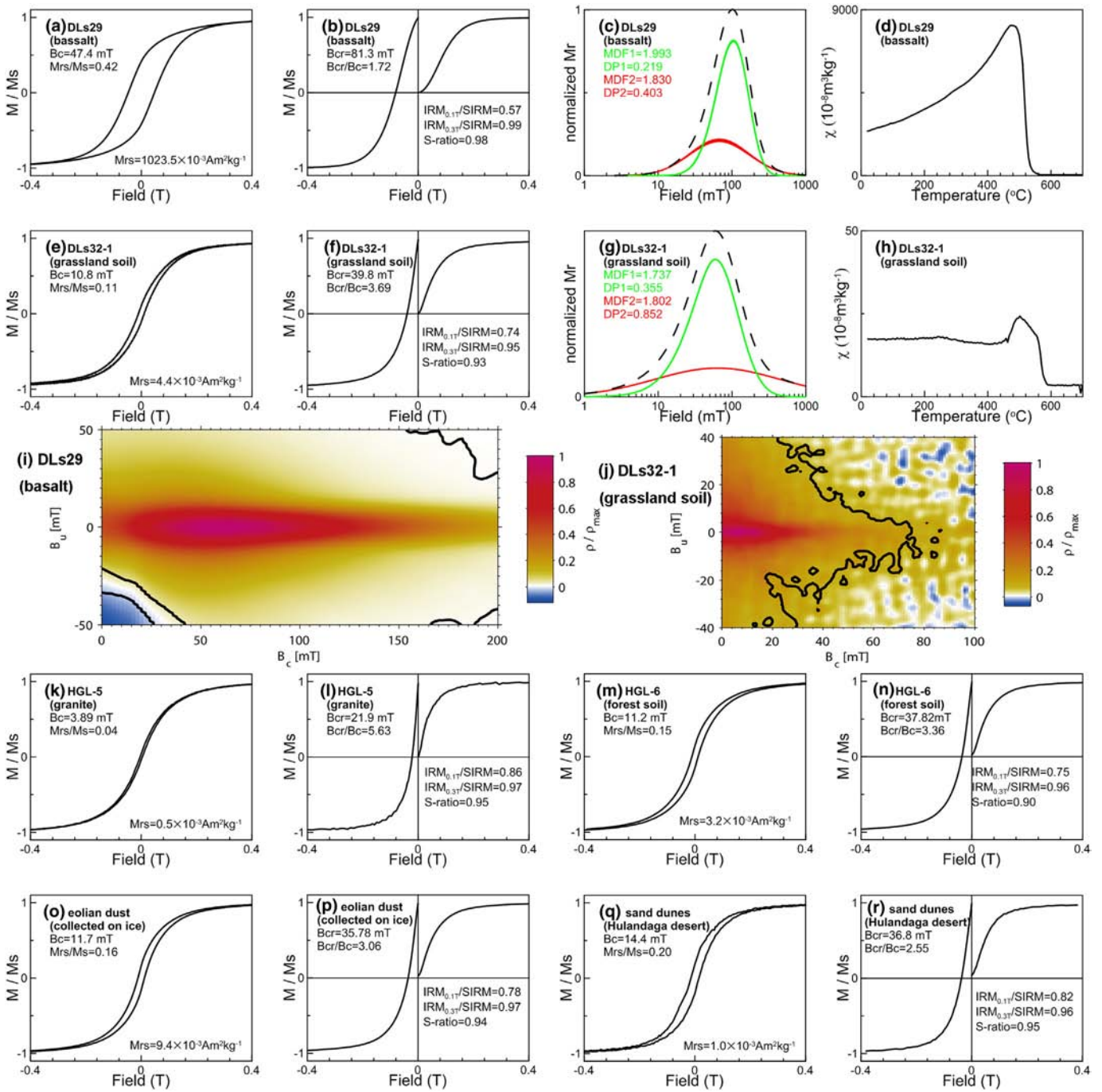


Fig. 6. Rock magnetic results for representative catchment samples, including hysteresis loops (a, e, k, m, o, q), IRM acquisition and DC demagnetization curves (b, f, l, n, p, r), unmixing of the IRM acquisition curves (c, g), magnetic susceptibility vs temperature curves (d, h; for clarity, only heating curves are shown), and first-order reversal diagrams (FORCs) which are calculated with $SF = 5$ (i, j). The hysteresis loops and IRM curves, which are obtained in the applied field up to 1 T, are cut off at 0.4 T for clarity.

2014). FORC diagram for sample DL1175 (Fig. 3r) has SD-like distribution with concentric contours and considerable vertical spread. These features are different from biogenic SD magnetite from the Holocene Warm Period sediments in the DL04 core, which typically has low magnetic interaction fields (Liu et al., 2015). Although the FORC diagram for DL1175 has some similarities with iron sulfides like greigite, our SEM, TEM and EDS results exclude this possibility (discussed below in Section 4.2.3, Fig. 5). In contrast, FORC diagrams for DL930 (Fig. 3l) and DL1010 (Fig. 3o) have peaks at ~20 mT. The contours remain open and intersect with the B_u axis. This suggests the dominance of PSD particles.

4.2.2. χ -T and $SIRM_{20 K, 2.5 T}$ -T results

χ -T curves for all three representative samples decrease sharply at 550–600 °C (Fig. 3j, m, p), which indicates the dominance of (titano-)magnetite as the main magnetic carrier. The peak or hump at around 450–500 °C may result from the neo-formation of magnetite grains from iron-containing minerals silicates, clays or carbonates (Deng et al., 2001; Zhang et al., 2014; Pan et al., 2000). This is consistent with significant increases of magnetic susceptibility in the cooling curves compared with their heating counterparts (insets in Fig. 3j, m, p). Inflection at lower temperatures, which may indicate the decomposition of thermally unstable

magnetic minerals (e.g., goethite or greigite), is not observed in the Dali Lake sediments.

Samples DL930 and DL1010 exhibit detectable Verwey transitions at ~120 K (Fig. 3k, n), which confirms the dominance of magnetite (Verwey, 1939). The Verwey transition for sample DL1175 is less visible (Fig. 3q). This could be attributed to less PSD and MD magnetite in Unit 1. The Verwey transition may also be suppressed due to inclusion of titanium in crystal lattice or oxidation of magnetite (Özdemir et al., 1993).

4.2.3. SEM, TEM and EDS results

The SEM and TEM observations coupled with EDS analysis for the representative samples from Unit 1 indicate that the dominant magnetic mineral is titanomagnetite, as shown by the scanning map (Fig. 5a, b1–b6) and spectra (Fig. 5c–f) of sample DL1151. Titanomagnetite in Dali Lake has a general grain size in order of μm , and some crystals are still embedded in silicates (likely clay minerals). Although sulfide exists in DL1174, TEM imaging and EDS suggest sulfide in calcium sulfate (Fig. 5g–i) rather than iron sulfides. No iron sulfide was found in SEM or TEM analyses.

4.3. Magnetic properties of catchment samples

The basalt, which is most highly magnetized among all potential magnetic sources, has SD-like behavior characterized by high B_c (~50 mT) and B_{cr} (~80 mT) (Fig. 6a, b), projection on the Day plot near the SD area (Day et al., 1977) (Fig. 4), elongated contours in the FORC diagram (Fig. 6i), and a narrowly distributed (DP = 0.219) main magnetic component centered at ~98 mT (Fig. 6c). Sharp decrease of χ at 500–550 °C during heating demonstrates the dominance of low-titanium titanomagnetite in the basalt (Fig. 6d).

Magnetic results from the surface soil samples indicate the dominance of PSD particles (Fig. 6j). These samples have narrow hysteresis loops with low B_c values of ~10 mT (Fig. 6e, m). On the Day plot, surface soil samples cluster around the lower right-hand corner of the PSD area (Fig. 4). Curie points calculated from the χ - T curves are generally near 580 °C (Fig. 6h). Moreover, the unmixing result suggests a widely distributed (DP = 0.355) main magnetic component (Fig. 6g).

The eolian dust has an SIRM value of $\sim 10^{-2} \text{ Am}^2 \text{ kg}^{-1}$ (Fig. 6o), which is higher than the soils but lower than the basalt. The magnetic properties of eolian dust are similar to surface soils from the grassland and the forest. Granite at the headwater area has a very low magnetic remanence value (Fig. 6k). Its projection on the Day plot covers the PSD and MD area (Fig. 4), consistent with its “thin” hysteresis loop. Another magnetically weak source is the sand from sand dunes in Hulandaga Desert (Fig. 6q).

4.4. XRD results

Minerals were identified based on the following main peaks: muscovite: 9.95 Å and 3.32 Å, fraipontite: 7.07 Å, quartz/silica: 4.26 Å and 3.34 Å, sanidine: 3.245 Å, anorthite: 3.21–3.22 Å, rutile: 3.20 Å, albite: 3.18–3.19 Å, calcite: 3.03 Å, augite: 3.00–2.99 Å, titanomagnetite, 2.56 Å. All the three core sediments have quartz, which is common for bulk samples (Fig. 7b, e, f). Calcite and anorthite are found in DL930 and DL1050 (Fig. 7e, f), which may result from high lake productivity. In contrast, sanidine, albite and augite exist in DL1174, together with contribution from johannsenite (Fig. 7b). This implies a low weathering during the sedimentation of Unit 1.

The basalt sample DLS29 (Fig. 7a) has a rather different composition compared to all other catchment and core samples. It is dominated by augite, clinoferrrosilite and anorthite, which is consistent with its mafic origin. Titanomagnetite is also found in DLS29 (Fig. 7a). The soil samples DLS32-1 and HGL-6 both show a dominance of silica, with contribution of albite and orthoclase (Fig. 7c, d). The other catchment samples also

have a large proportion of quartz. Various feldspars like sanidine and orthoclase exist in these weather-resistant samples (Fig. 7g–i).

5. Discussion

5.1. Origin of magnetic minerals deposited in Dali Lake

Of all the samples collected in the Dali Lake catchment, granite is the least magnetized. Therefore, it is probably not the main source of magnetic minerals in the DL04 core. The contribution of sand dunes south of the lake is also minor, considering the general fine grain size of core sediments except for the bottom 30 cm. Another source to preclude as main source is eolian dust. First, sedimentation accumulation rate in Dali Lake is ~75 cm/kyr during the last deglaciation and up to ~100 cm/kyr from 11.5 ka to 15.3 ka, while the average loess accumulation rate in the Loess Plateau is usually less than 10 cm/kyr. Second, Dali Lake is about 1000 km northeast of the Loess Plateau. Chen et al. (2013) studied the magnetic source of Gonghai Lake (38°54' N, 112°14' E) located just at the northern margin of the Loess Plateau and concluded that eolian dust was not a major magnetic contributor. Considering the position of Dali Lake further to the northeast, eolian dust from dust sources (the Gobi and deserts in northwestern China and central Asia) will make only a minor contribution (if any) to the detrital sediments in Dali Lake.

The main magnetic minerals in the DL04 core are originated from either basalt or surface soils nearby the Dali Lake. Detailed comparison of magnetic concentration, grain size and mineralogy of core sediments with those from the catchment may provide helpful constraints on the magnetic mineral sources. Core sediments from Unit 1 have magnetic features that highly resemble those of the basalt in the catchment. The similarities include SD-like hysteresis properties, narrow distribution of main magnetic component, and titanomagnetite as the main magnetic mineral (Figs. 3, 4, 6). Moreover, XRD results are also consistent with an inferred low weathering extent. We therefore infer that core sediments in Unit 1 are likely to originate from bedrock erosion.

The core sediments in Dali Lake changed dramatically from sands in Unit 1 to clays and silty clays in Unit 2 and upward at 11.5 m. This obvious grain size change may reflect changing erosion process in the catchment area. In Units 2 and 3, the magnetic concentration is much lower, while magnetic grain size is coarser with more PSD-like characteristics. In addition, core sediments from Units 2 and 3 show similar magnetic characteristics as surface soils in the catchment, characterized by widely distributed main magnetic component, PSD-like FORC diagrams and probably more SP contribution (Figs. 3, 6). We infer that magnetic minerals in Unit 2 mainly originate from erosion of surface soils in the catchment area.

5.2. Links between the DL04 core and paleoclimate changes during the last deglaciation

The different origins of detrital magnetic minerals, from bedrock erosion or surface soils, reflect contrasting catchment erosion processes around the lake during cold and warm periods. These processes were controlled by paleoclimate changes in the Dali Lake region during the last deglaciation. We therefore explore the climatic variability of the lower three units, Unit 1 to Unit 3, in this context.

5.2.1. Paleoclimatic interpretation of Unit 1 (15.90–15.32 ka)

Unit 1 represents the period just after the Last Glacial Maximum (Fig. 8). We infer that strong freeze–thaw activity due to ice cover prompts physical weathering of bedrock during this cold period. In addition, pollen data from Xiarinur Lake (42°37' N, 115°28' E), which is ~150 km southwest of Dali Lake, indicates sparse vegetation cover in the area during this period (Tang et al., 2015). This would have allowed weathering and transportation of lithogenic inputs directly into Dali Lake, without strong chemical weathering. Titanomagnetite is common

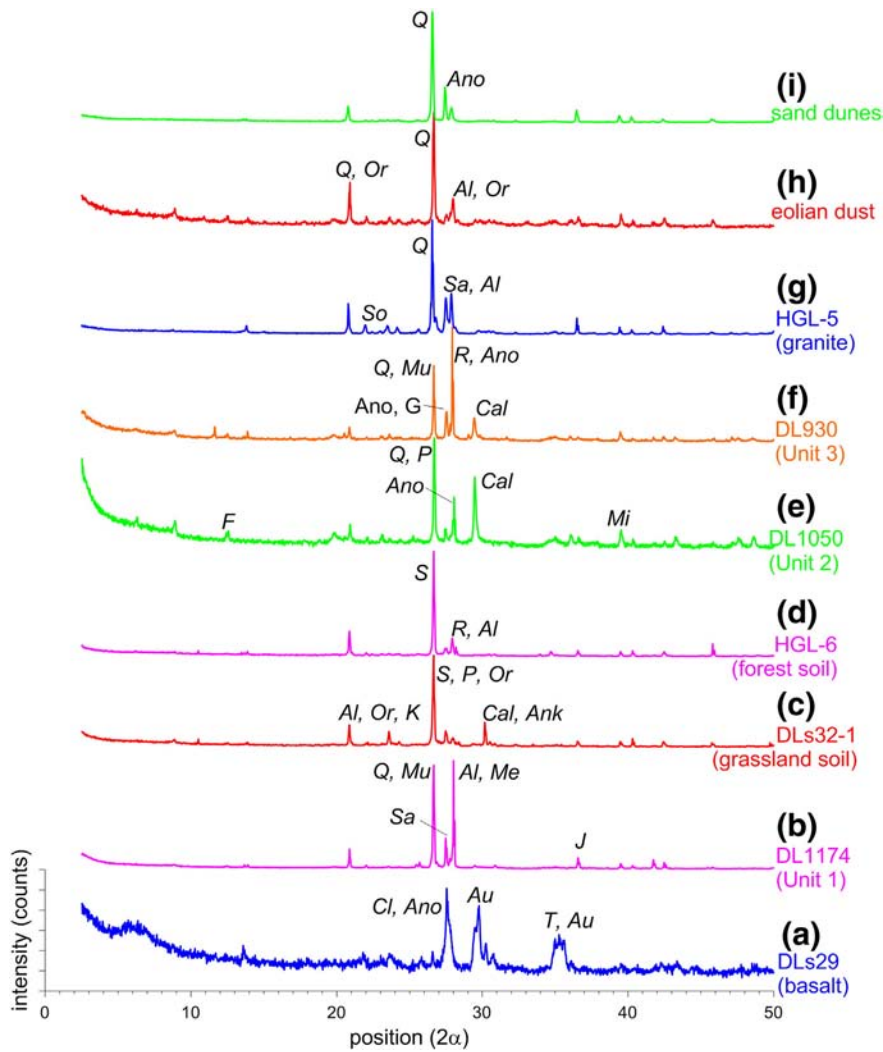


Fig. 7. X-ray diffraction results of bulk samples from representative DL04 core sediments and catchment samples. The scanning angle (2α) range is 0° – 90° , but for clarity only the parts from 0° to 50° are displayed. Abbreviations of minerals are: F for ferrihydrite, J for johannsenite, P for polyolithionite, Q for quartz, R for rutile, S for silica, T for titanomagnetite, Al for albite, Au for augite, Ank for ankerite, An for anorthoclase, Cl for clinoferrosilite, Cal for calcite, Me for merinoite, Mi for mica, Mu for muscovite, Or for orthite, Sa for sanidine, So for sodalite.

in mafic igneous rocks. Given the abundance of vesicular basalt in the catchment, it is reasonable to infer that a highly magnetic layer mainly from basalt erosion was preserved in the DL04 core.

The rapid climate fluctuations documented in Unit 1 can be tentatively correlated with Heinrich event 1, which has also been recovered in the Atlantic (Bond et al., 1997; Heinrich, 1988), the Greenland ice cores (Dansgaard et al., 1993), and in the East Asian loess (Porter and An, 1995), stalagmites (Wang et al., 2001) and lake sediments (Jin et al., 2015). Our findings suggest that during this period, the Dali Lake region may have experienced strong physical erosion, which was likely the result of glacial conditions in northern China.

5.2.2. Paleoclimatic interpretation of Unit 2 (15.32–12.67 ka)

Unit 2 coincides within age error with the Bølling–Allerød warm period (Fig. 8). The ameliorating local climate during this period would have enhanced pedogenesis, which favored the formation of effective remanence carriers (SD and small PSD ferrimagnetic particles) (Deng et al., 2005; Zhou et al., 1990). The newly formed surface soils would have been easily eroded and transported into the lake by runoffs and rivers in the catchment. This model is consistent with our observation

of abundant PSD magnetite with SP contribution in Unit 2 (Figs. 2, 3d–f, m–o).

The Bølling–Allerød warm period in our record is not as obvious as in Chinese speleothems and Greenland ice core (Fig. 8). The relatively small responding amplitude in East Asia to this millennial-scale change was also reported in recent studies on Chinese loess (Lu et al., 2013; Sun et al., 2015) and lake sediments (Liu et al., 2014). The insensitive response may originate from a climate threshold (Liu et al., 2014) or local hydrological changes.

5.2.3. Paleoclimatic interpretation of Unit 3 (12.67–11.56 ka)

The Younger Dryas may represent the best studied millennial-scale events during Quaternary (Broecker et al., 2010). Unit 3 of our magnetic series can be correlated within age error with this event. During this short cold and dry period, magnetic concentration in Dali Lake decreased and the magnetic grain size was finer than that during the Bølling–Allerød warm period. This may be attributed to less fluvial and runoff transportation.

The amplitudes of variations during the Younger Dryas are much smaller than that after the Last Glacial Maximum, which is also evident in the stacked grain size data from the Chinese loess (Yang and Ding,

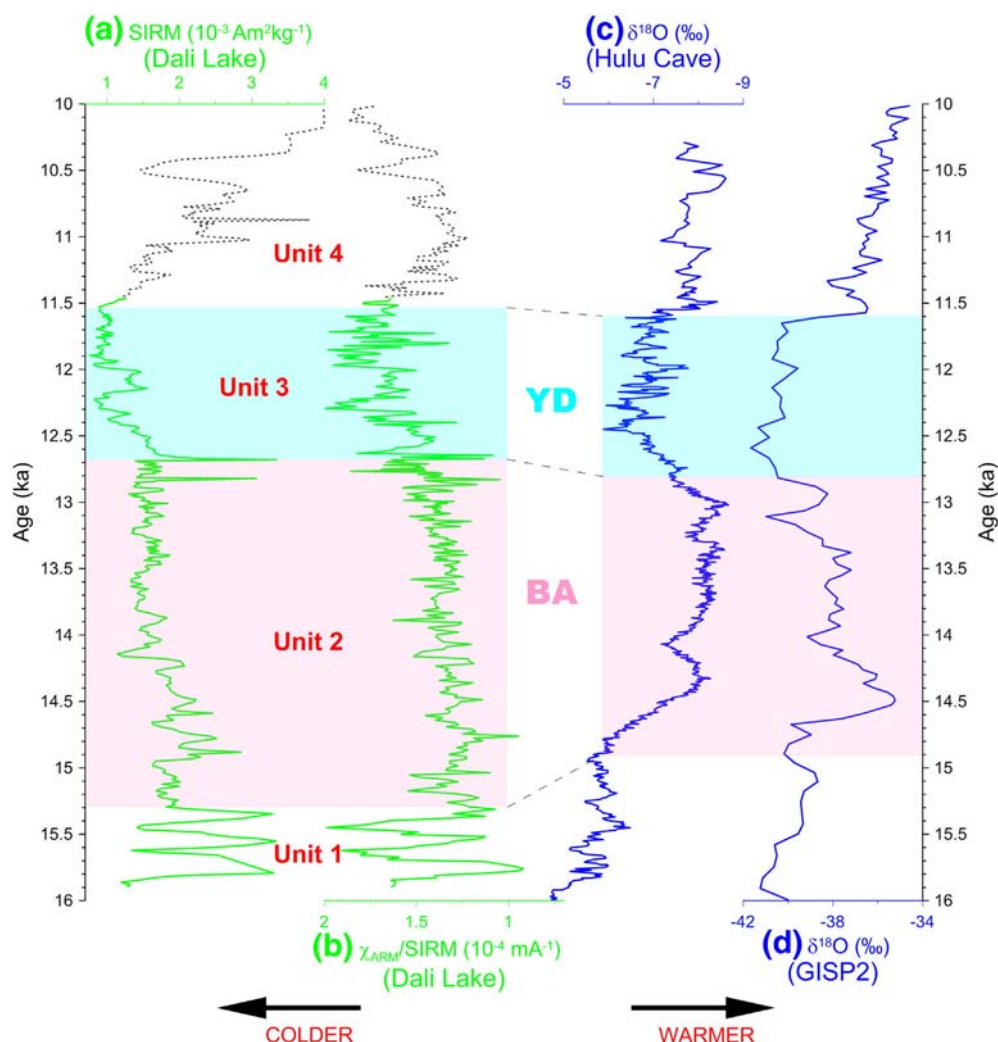


Fig. 8. Correlation of the Dali Lake results with other paleoclimate records during the last deglaciation. a, Magnetic concentration of Dali Lake sediments, represented by SIRM; b, magnetic grain size of Dali Lake, represented by the ratio value of $\chi_{ARM}/SIRM$. Rock magnetic data over the time interval of 11.5–10 ka, shown by dotted lines in Fig. 7a and b, are after Liu et al. (2015). c, Stalagmite $\delta^{18}O$ record in Hulu Cave, southern China (Wang et al., 2001), data downloaded from <https://www.ncdc.noaa.gov/paleo/study/5426>; d, $\delta^{18}O$ record in Greenland ice core (Groote and Stuiver, 1997), downloaded from <http://www.ncdc.noaa.gov/paleo/study/17796>. YD is the abbreviation for Younger Dryas, and BA is for Bølling–Allerød.

2014) and the speleothem $\delta^{18}O$ record in Kulishu Cave near Beijing (Ma et al., 2012). These findings indicate that the East Asian summer monsoon weakened after the Bølling–Allerød warming period. This weakening, however, was probably not as large as that seen during glacial conditions based on magnetic properties. One possible explanation is, as proposed by Ma et al. (2012), that the North Atlantic changes did not supersede the orbital forcing. However, the reason for the amplitude difference deserves further investigation.

Anomalies during the Younger Dryas are documented in the DL04 record at ~12.0–12.2 ka and ~12.6 ka. Such a climatically unstable Younger Dryas has previously been reported in northern Europe (Ebbesen and Hald, 2004) and in East Asia (Ma et al., 2012; Zhou et al., 1996), which confirms the capability of our magnetic record in documenting high-resolution climate features. In addition, a good correlation between Dali Lake and the North Atlantic during the Younger Dryas supports the North Atlantic forcing of millennial-scale variability in the semi-arid East Asia (Wang et al., 2001).

6. Conclusions

Systematic rock magnetic analysis reveals that the DL04 core during the last deglaciation can be divided into four units based on changes in lithology and magnetic properties. Unit 1 (15.90–15.32 ka) is

dominated by highly magnetic SD-like titanomagnetite from the surrounding basalt bedrock in the catchment. Ice cover under cold and dry conditions in Dali Lake area led to erosion of bedrock with little chemical weathering. Magnetic minerals in Unit 2 (15.32–12.67 ka) and Unit 3 (12.67–11.56 ka) originate mostly from surface soils in the catchment. The Bølling–Allerød warm period and Younger Dryas cold event, respectively, are documented in our record and can be correlated in time within error with previous studies. Overall, our magnetic record documents paleoclimatically controlled erosion and transportation mechanisms influencing Dali Lake during the last deglaciation.

Acknowledgments

We thank Jiawei Fan, Ruilin Wen and Dayou Zhai for help during fieldwork and Junyi Ge for useful discussions. Chunxia Zhang is gratefully acknowledged for her help during the XRD analysis. We are also grateful to Eric Font, Xisheng Wang, and Editor Paul Hesse for their insightful comments and suggestions which significantly improved the manuscript. This research was supported by the NSFC grants 41574061, 41330104 and the 973 program grant 2012CB821900. J.X. was supported by the 973 program grant 2010CB833400 and the NSFC grant 41130101. C.D. acknowledges further support from the CAS Bairen Program.

References

- An, Z.S., Wu, G.X., Li, J.P., Sun, Y.B., Liu, Y.M., Zhou, W.J., Cai, Y.J., Duan, A.M., Li, L., Mao, J.Y., Cheng, H., Shi, Z.G., Tan, L.C., Yan, H., Ao, H., Chang, H., Feng, J., 2015. Global monsoon dynamics and climate change. *Annu. Rev. Earth Planet. Sci.* 43, 29–77. <http://dx.doi.org/10.1146/annurev-earth-060313-054623>.
- Bond, G., Broecker, W., Johnsen, S., McManus, J., Labeyrie, L., Jouzel, J., Bonani, G., 1993. Correlations between climate records from North Atlantic sediments and Greenland ice. *Nature* 365, 143–147. <http://dx.doi.org/10.1038/365143a0>.
- Bond, G., Showers, W., Cheseby, M., Lotti, R., Almasi, P., deMenocal, P., Priore, P., Cullen, H., Hajdas, I., Bonani, G., 1997. A pervasive millennial-scale cycle in North Atlantic Holocene and glacial climates. *Science* 278, 1257–1266. <http://dx.doi.org/10.1126/science.278.5341.1257>.
- Broecker, W.S., Denton, G.H., Edwards, R.L., Cheng, H., Alley, R.B., Putnam, A.E., 2010. Putting the Younger Dryas cold event into context. *Quat. Sci. Rev.* 29, 1078–1081. <http://dx.doi.org/10.1016/j.quascirev.2010.02.019>.
- Chen, F.H., Liu, J.B., Xu, Q.H., Li, Y.C., Chen, J.H., Wei, H.T., Liu, Q.S., Wang, Z.L., Cao, X.Y., Zhang, S.R., 2013. Environmental magnetic studies of sediment cores from Gonghai Lake: implications for monsoon evolution in North China during the late glacial and Holocene. *J. Paleolimnol.* 49, 447–464. <http://dx.doi.org/10.1007/s10933-012-9677-3>.
- Dansgaard, W., Johnsen, S.J., Clausen, H.B., Dahljensen, D., Gundestrup, N.S., Hammer, C.U., Hvidberg, C.S., Steffensen, J.P., Sveinbjornsdottir, A.E., Jouzel, J., Bond, G., 1993. Evidence for general instability of past climate from a 250-kyr ice core record. *Nature* 364, 218–220. <http://dx.doi.org/10.1038/364218a0>.
- Day, R., Fuller, M., Schmidt, V.A., 1977. Hysteresis properties of titanomagnetites: grain-size and compositional dependence. *Phys. Earth Planet. Inter.* 13, 260–267. [http://dx.doi.org/10.1016/0031-9201\(77\)90108-X](http://dx.doi.org/10.1016/0031-9201(77)90108-X).
- Deng, C.L., Shaw, J., Liu, Q.S., Pan, Y.X., Zhu, R.X., 2006. Mineral magnetic variation of the Jingbian loess/paleosol sequence in the northern Loess Plateau of China: implications for Quaternary development of Asian aridification and cooling. *Earth Planet. Sci. Lett.* 241, 248–259. <http://dx.doi.org/10.1016/j.epsl.2005.10.020>.
- Deng, C.L., Vidic, N.J., Verosub, K.L., Singer, M.J., Liu, Q.S., Shaw, J., Zhu, R.X., 2005. Mineral magnetic variation of the Jiaodao Chinese loess/paleosol sequence and its bearing on long-term climatic variability. *J. Geophys. Res.* 110, B03103. <http://dx.doi.org/10.1029/2004jb003451>.
- Deng, C.L., Zhu, R.X., Jackson, M.J., Verosub, K.L., Singer, M.J., 2001. Variability of the temperature-dependent susceptibility of the Holocene eolian deposits in the Chinese loess plateau: a pedogenesis indicator. *Phys. Chem. Earth* 26, 873–878. [http://dx.doi.org/10.1016/S1464-1895\(01\)00135-1](http://dx.doi.org/10.1016/S1464-1895(01)00135-1).
- Ding, Z.L., Derbyshire, E., Yang, S.L., Yu, Z.W., Xiong, S.F., Liu, T.S., 2002. Stacked 2.6-Ma grain size record from the Chinese loess based on five sections and correlation with the deep-sea $\delta^{18}\text{O}$ record. *Paleoceanography* 17. <http://dx.doi.org/10.1029/2001PA000725>.
- Ding, Z.L., Sun, J.M., Yu, Z.W., Liu, D.S., 1998. Chronology of environmental events over East Asia during the past 130 ka. *Chin. Sci. Bull.* 43, 1761–1769. <http://dx.doi.org/10.1007/b02883368>.
- Ebbesen, H., Hald, M., 2004. Unstable Younger Dryas climate in the northeast North Atlantic. *Geology* 32, 673–676. <http://dx.doi.org/10.1130/g20653.1>.
- Egli, R., 2003. Analysis of the field dependence of remanent magnetization curves. *J. Geophys. Res.* 108. <http://dx.doi.org/10.1029/2002jb002023> (EPM4-1–EPM4-25).
- Fan, J., Xiao, J., Wen, R., Zhai, D., Wang, X., Cui, L., Itoh, S., 2015. Holocene environment variations recorded by stable carbon and nitrogen isotopes of sedimentary organic matter from Dali Lake in inner Mongolia (in Chinese with English abstract). *Quat. Sci.* 35, 856–870. <http://dx.doi.org/10.1192/qj.issn.1001-7410.2015.04.08>.
- Groote, P.M., Stuiver, M., 1997. Oxygen 18/16 variability in Greenland snow and ice with 10^{-3} to 10^5 -year time resolution. *J. Geophys. Res. Oceans* 102, 26455–26470. <http://dx.doi.org/10.1029/97jc00880>.
- Guo, Z.T., Liu, T.S., Guiot, J., Wu, N., Lu, H., Han, J., Liu, J., Gu, Z., 1996. High frequency pulses of East Asian monsoon climate in the last two glaciations: link with the North Atlantic. *Clim. Dyn.* 12, 701–709. <http://dx.doi.org/10.1007/s003820050137>.
- Guo, Z.T., Ruddiman, W.F., Hao, Q.Z., Wu, H.B., Qiao, Y.S., Zhu, R.X., Peng, S.Z., Wei, J.J., Yuan, B.Y., Liu, T.S., 2002. Onset of Asian desertification by 22 Myr ago inferred from loess deposits in China. *Nature* 416, 159–163. <http://dx.doi.org/10.1038/416159a>.
- Hao, Q.Z., Wang, L., Oldfield, F., Guo, Z.T., 2015. Extra-long interglacial in Northern Hemisphere during MISs 15–13 arising from limited extent of Arctic ice sheets in glacial MIS 14. *Sci. Rep.* 5. <http://dx.doi.org/10.1038/srep12103>.
- Heinrich, H., 1988. Origin and consequences of cyclic ice rafting in the Northeast Atlantic-Ocean during the past 130,000 years. *Quat. Res.* 29, 142–152. [http://dx.doi.org/10.1016/0033-5894\(88\)90057-9](http://dx.doi.org/10.1016/0033-5894(88)90057-9).
- Heller, F., Liu, T.S., 1984. Magnetism of Chinese loess deposits. *Geophys. J. R. Astron. Soc.* 77, 125–141. <http://dx.doi.org/10.1111/j.1365-246X.1984.tb01928.x>.
- Heslop, D., Roberts, A.P., 2012. Estimation of significance levels and confidence intervals for first-order reversal curve distributions. *Geochem. Geophys. Geosyst.* 13, Q12240. <http://dx.doi.org/10.1029/2012GC004115>.
- Jin, Z.D., An, Z.S., Yu, J.M., Li, F.C., Zhang, F., 2015. Lake Qinghai sediment geochemistry linked to hydroclimate variability since the last glacial. *Quat. Sci. Rev.* 122, 63–73. <http://dx.doi.org/10.1016/j.quascirev.2015.05.015>.
- King, J.W., Channell, J.E.T., 1991. Sedimentary magnetism, environmental magnetism, and magnetostratigraphy. *Rev. Geophys.* 29, 358–370.
- Liu, J.B., Chen, F.H., Chen, J.H., Xia, D.S., Xu, Q.H., Wang, Z.L., Li, Y.C., 2011. Humid medieval warm period recorded by magnetic characteristics of sediments from Gonghai Lake, Shanxi, North China. *Chin. Sci. Bull.* 56, 2464–2474. <http://dx.doi.org/10.1007/s11434-011-4592-y>.
- Liu, X.J., Colman, S.M., Brown, E.T., An, Z.S., Zhou, W.J., Jull, A.J.T., Huang, Y.S., Cheng, P., Liu, W.G., Xu, H., 2014. A climate threshold at the eastern edge of the Tibetan plateau. *Geophys. Res. Lett.* 41, 5598–5604. <http://dx.doi.org/10.1002/2014gl060833>.
- Liu, S.Z., Deng, C.L., Xiao, J.L., Li, J.H., Paterson, G.A., Chang, L., Yi, L., Qin, H.F., Pan, Y.X., Zhu, R.X., 2015. Insolation driven biomagnetic response to the Holocene warm period in semi-arid East Asia. *Sci. Rep.* 5, 8001. <http://dx.doi.org/10.1038/srep08001>.
- Lu, H.Y., Yi, S.W., Liu, Z.Y., Mason, J.A., Jiang, D.B., Cheng, J., Stevens, T., Xu, Z.W., Zhang, E.L., Jin, L.Y., Zhang, Z.H., Guo, Z.T., Wang, Y., Otto-Bliesner, B., 2013. Variation of East Asian monsoon precipitation during the past 21 kyr, and potential CO₂ forcing. *Geology* 41, 1023–1026. <http://dx.doi.org/10.1130/g34488.1>.
- Ma, Z.B., Cheng, H., Tan, M., Edwards, R.L., Li, H.C., You, C.F., Duan, W.H., Wang, X., Kelly, M.J., 2012. Timing and structure of the Younger Dryas event in northern China. *Quat. Sci. Rev.* 41, 83–93. <http://dx.doi.org/10.1016/j.quascirev.2012.03.006>.
- Özdemir, Ö., Dunlop, D.J., Moskowitz, B.M., 1993. The effect of oxidation on the Verwey transition in magnetite. *Geophys. Res. Lett.* 20, 1671–1674. <http://dx.doi.org/10.1029/93GL01483>.
- Pan, Y.X., Zhu, R.X., Banerjee, S.K., Gill, J., Williams, Q., 2000. Rock magnetic properties related to thermal treatment of siderite: behavior and interpretation. *J. Geophys. Res. Solid Earth* 105, 783–794. <http://dx.doi.org/10.1029/1999jb900358>.
- Porter, S.C., An, Z.S., 1995. Correlation between climate events in the North Atlantic and China during the last glaciation. *Nature* 375, 305–308. <http://dx.doi.org/10.1038/375305a0>.
- Roberts, A.P., Heslop, D., Zhao, X., Pike, C.R., 2014. Understanding fine magnetic particle systems through use of first-order reversal curve diagrams. *Rev. Geophys.* 52. <http://dx.doi.org/10.1002/2014RG000462>.
- Roberts, A.P., Pike, C.R., Verosub, K.L., 2000. First-order reversal curve diagrams: a new tool for characterizing the magnetic properties of natural samples. *J. Geophys. Res.* 105, 28461–28475. <http://dx.doi.org/10.1029/2000jb900326>.
- Ruddiman, W.F., 2014. *Earth's Climate: Past and Future*. third ed. Freeman, New York.
- Stuiver, M., Grootes, P.M., Braziunas, T.F., 1995. The GISP2 $\delta^{18}\text{O}$ climate record of the past 16,500 years and the role of the sun, ocean, and volcanoes. *Quat. Res.* 44, 341–354. <http://dx.doi.org/10.1006/qres.1995.1079>.
- Sun, Y.B., Kutzbach, J., An, Z.S., Clemens, S., Liu, Z.Y., Liu, W.G., Liu, X.D., Shi, Z.G., Zheng, W.P., Liang, L.J., Yan, Y., Li, Y., 2015. Astronomical and glacial forcing of East Asian summer monsoon variability. *Quat. Sci. Rev.* 115, 132–142. <http://dx.doi.org/10.1016/j.quascirev.2015.03.0>.
- Tang, L., Wang, X., Zhang, S., Chu, G., Chen, Y., Pei, J., Sheng, M., Yang, Z., 2015. High-resolution magnetic and palynological records of the last deglaciation and Holocene from Lake Xiarinur in the Hunshandake Sandy Land, Inner Mongolia. *The Holocene* 25, 844–856. <http://dx.doi.org/10.1177/0959683615571426>.
- Thouveny, N., Debeaulieu, J.L., Bonifay, E., Creer, K.M., Guiot, J., Icole, M., Johnsen, S., Jouzel, J., Reille, M., Williams, T., Williamson, D., 1994. Climate variations in Europe over the past 140 kyr deduced from rock magnetism. *Nature* 371, 503–506. <http://dx.doi.org/10.1038/371503a0>.
- Verwey, E., 1939. Electronic conduction of magnetite (Fe₃O₄) and its transition point at low temperatures. *Nature* 144, 327–328. <http://dx.doi.org/10.1038/144327b0>.
- Wang, Y.J., Cheng, H., Edwards, R.L., An, Z.S., Wu, J.Y., Shen, C.C., Dorale, J.A., 2001. A high-resolution absolute-dated Late Pleistocene monsoon record from Hulu Cave, China. *Science* 294, 2345–2348. <http://dx.doi.org/10.1126/science.1064618>.
- Xiao, J.L., Chang, Z.G., Si, B., Qin, X.G., Itoh, S., Lomtatidze, Z., 2009. Partitioning of the grain-size components of Dali Lake core sediments: evidence for lake-level changes during the Holocene. *J. Paleolimnol.* 42, 249–260. <http://dx.doi.org/10.1007/s10933-008-9274-7>.
- Xiao, J.L., Si, B., Zhai, D.Y., Itoh, S., Lomtatidze, Z., 2008. Hydrology of Dali Lake in central-eastern Inner Mongolia and Holocene East Asian monsoon variability. *J. Paleolimnol.* 40, 519–528. <http://dx.doi.org/10.1007/s10933-007-9179-x>.
- Yang, S.L., Ding, Z.L., 2014. A 249 kyr stack of eight loess grain size records from northern China documenting millennial-scale climate variability. *Geochem. Geophys. Geosyst.* 15, 798–814. <http://dx.doi.org/10.1002/2013gc005113>.
- Yuan, D.X., Cheng, H., Edwards, R.L., Dykoski, C.A., Kelly, M.J., Zhang, M.L., Qing, J.M., Lin, Y.S., Wang, Y.J., Wu, J.Y., Dorale, J.A., An, Z.S., Cai, Y.J., 2004. Timing, duration, and transitions of the Last Interglacial Asian Monsoon. *Science* 304, 575–578. <http://dx.doi.org/10.1126/science.1091220>.
- Zhang, Y., Guo, Z.T., Deng, C.L., Zhang, S.Q., Wu, H.B., Zhang, C.X., Ge, J.Y., Zhao, D.A., Li, Q., Song, Y., Zhu, R.X., 2014. The use of fire at Zhoukoudian: evidence from magnetic susceptibility and color measurements. *Chin. Sci. Bull.* 59, 1013–1020. <http://dx.doi.org/10.1007/s11434-013-0111-7>.
- Zhou, W.J., Donahue, D.J., Porter, S.C., Jull, T.A., Li, X.Q., Stuiver, M., An, Z.S., Matsumoto, E., Dong, G.G., 1996. Variability of monsoon climate in East Asia at the end of the last glaciation. *Quat. Res.* 46, 219–229. <http://dx.doi.org/10.1006/qres.1996.0062>.
- Zhou, W.J., Head, M.J., Lu, X.F., An, Z.S., Jull, A.J.T., Donahue, D., 1999. Teleconnection of climatic events between East Asia and polar, high latitude areas during the last deglaciation. *Palaeogeogr. Palaeoclimatol. Palaeoecol.* 152, 163–172. [http://dx.doi.org/10.1016/s0031-0182\(99\)00041-3](http://dx.doi.org/10.1016/s0031-0182(99)00041-3).
- Zhou, L.P., Oldfield, F., Wintle, A.G., Robinson, S.G., Wang, J.T., 1990. Partly pedogenic origin of magnetic variations in Chinese loess. *Nature* 346, 737–739. <http://dx.doi.org/10.1038/346737a0>.